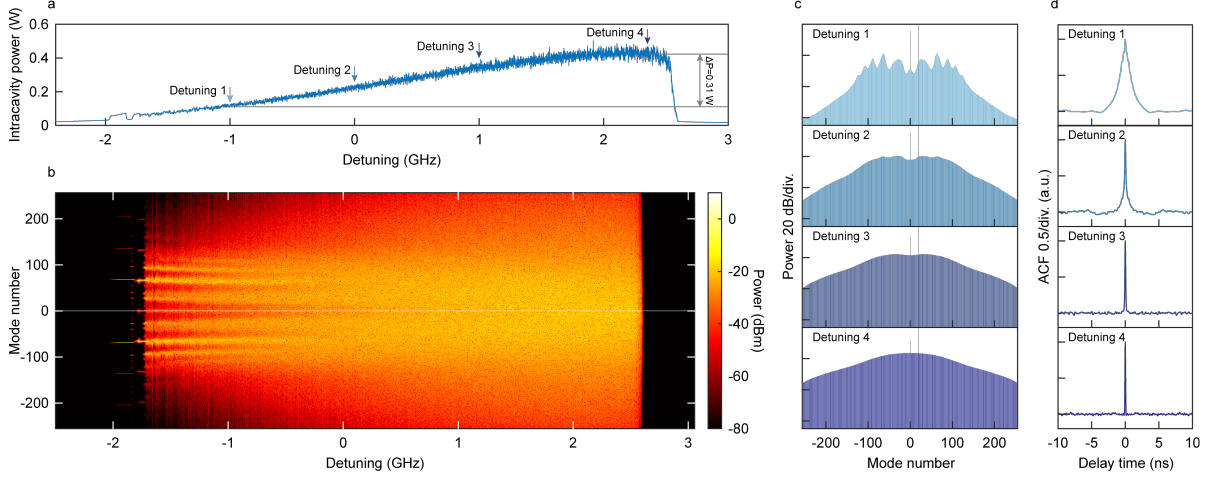# Breaking the temporal and frequency congestion of LiDAR by parallel chaos

In the format provided by the authors and unedited

CONTENTS

1

I. SUPPLEMENTARY NOTE I: THE NUMERICAL SIMULATION OF THE CHAOTIC COMB STATE

Supplementary Fig. 1: **The simulation result for the chaotic comb state in the AlGaAsOI platform. a**, the evolution of average intracavity power when the pump laser sweeping from the blue-detuning side to the red-detuning side of a resonance. **b**, Simulation of the intracavity spectrum evolution when the pump laser sweeping. **c**, the spectra under different detuning condition marked in a. **d**,The ACFs of the 20th combline next to the pump mode under different detuning condition marked in a.

To compare the chaotic dynamic in various integrated optical nonlinear platform, simulations based on the Lugiato-Lefever equation

$$t_R \frac{\partial \mathrm{E}(t,\tau)}{\partial \mathrm{t}} = \left[-\left(\frac{\alpha}{2} - i\delta_0 \right) + iL \sum_{k>1} \frac{\beta_k}{k!} \left(i\frac{\partial}{\partial \tau} \right)^k \right] E + iL\gamma |E|^2 E + \sqrt{\theta} E_{\mathrm{in}} \qquad (1)$$

are employed. The symbol definition is same with that in Method. The LLE is solved numerically by the Runge-Kutta method. Parameters for different platform is shown in Supplementary Tab. 1, with a coupling condition of critical coupling.

Supplementary Fig. 1a and b show the intracavity power and spectrum evolution with the variation of the pump detuning in the AlGaAsOI microring respectively, where the pump power is set to 100 mW. As the intracavity power increasing with the pump sweeping into the resonance, the intracavity state undergoes the evolution from continuous wave state to the primary comb state, and finally evolves into the chaotic comb state [1, 2]. The

averaged spectra and autocorrelation functions (ACFs) for different detuning marked in Supplementary Fig. 1a are shown in Supplementary Fig. 1c and d. As the increase of the detuning, the spectrum turns flatter and a sharper ACF is obtained. To characterize the chaotic dynamic for different platforms, the full-width-half-max (FWHM) of the ACF before the intracavity state drop into the continuous wave state or the soliton state is recorded and the result is shown in Fig. 2f.

Compared with the experiment result shown in Fig. 2g, the detuning range of the chaotic comb state in simulation is much narrower. Typically, the detuning range of the comb state is influenced by the kerr and thermal induced resonant frequency shift [3, 4]. As the kerr effect is included in the simulation, the difference between the simulation and the experiment can be contributed to the remarkable intracavity thermal-optical effect in the AlGaAsOI microring, which shows one-order higher thermal-optical coefficient compared with SiN. The resonant frequency shift $\Delta\omega_p$ induced by the thermal effect can be expressed as [4]

$$|\Delta\omega_p| = k_{\text{thermal}} \ |\Delta P_{\text{cav}}| \tag{2}$$

The k_{thermal} is the thermal related coefficient and defined as $\frac{\alpha_{\text{thermal}} \ \omega_0 (dn/dT)}{n_g K_c}$, where $\alpha_{thermal}$ is the thermal absorption rate, ω_0 is the cold cavity resonance frequency, dn/dT is the thermal-optical coefficient, n_g is the group index and K_c is the thermal conductance of the microring. As shown in Supplementary Fig. 1a, the intracavity power will change by 0.31 W from the detuning 1 to the detuning 4 and the corresponding resonant frequency shift $\Delta\omega_p$ is estimated to be 33 GHz, which is much larger than the existence range shown in Supplementary Fig. 1a.

Supplementary Tab. I: Parameters of different platforms for simulation

Platform	FSR (GHz)	Radius (µm)	Nonlinear coeficient $(m^{-1}W^{-1})$	Intrisic Q-factor (Million)
AlGaAsOI	90	141	350	2
SiC [5]	100	175	3.95	5.6
GaN [6]	100	198	3.79	2.5
AlN [7]	100	217	0.58	2.5
SiN [8]	100	228	0.93	30

II. SUPPLEMENTARY NOTE II: POWER OF ECHO SIGNALS AND THE CORRESPONDING CROSS-CORRELATION OF EACH CHANNEL IN THE SINGLE PD MEASUREMENT
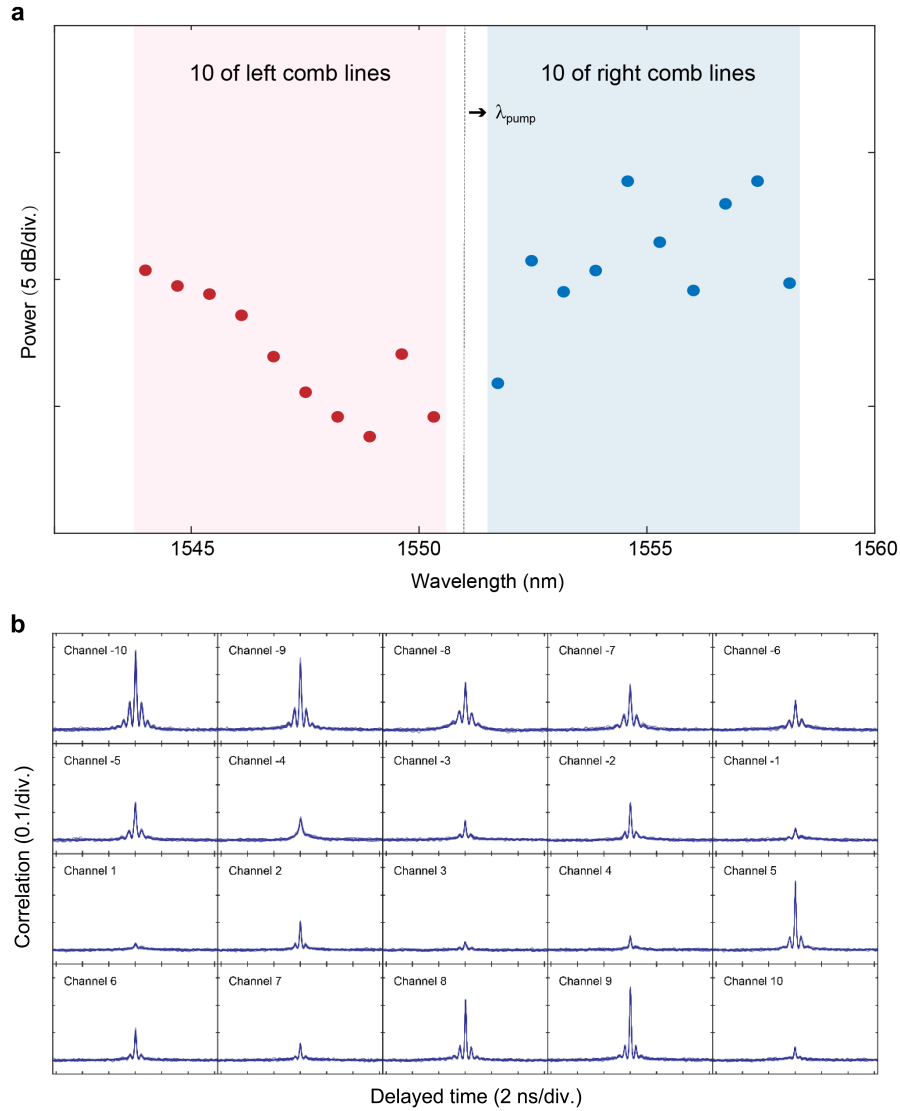
Supplementary Fig. 2: **The backscattered power of all 20 comb lines and the corresponding cross-correlation of each channel measured in the single PD detection. a** The red solid circles represent the backscattered power of the 10 comb lines that lie in the left side of the pump, while the blue solid circles represent the backscattered power of the 10 comb lines that lie in the right side of the pump. **b**, cross-correlation of each channel tested under simultaneous transmissions of 10 channels.

To prove that the uneven surface of the whiteboard will cause irregular backreflection, we also use the experimental setup as shown in Fig. 3a to emit a beam of each comb line in turn to the whiteboard and record the intensity of the reflected light of all 20 channels. Since we apply the monostatic detection scheme, the co-observed back reflection is related to the azimuthal distribution of the scattered power. Supplementary Fig. 2a shows that the irregular backreflection from the whiteboard influences the light power of all 20 channels that are finally collected in the receiving end, and its profile distribution is in agreement with the SNR results of all-20 channels after correlation processing in Fig. 3b. The raw correlation curves are depicted in Supplementary Fig. 2b.

III. SUPPLEMENTARY NOTE III: CHANNEL-BY-CHANNEL AUTO-CORRELATION OF THE PARALLEL CHAOTIC SOURCE
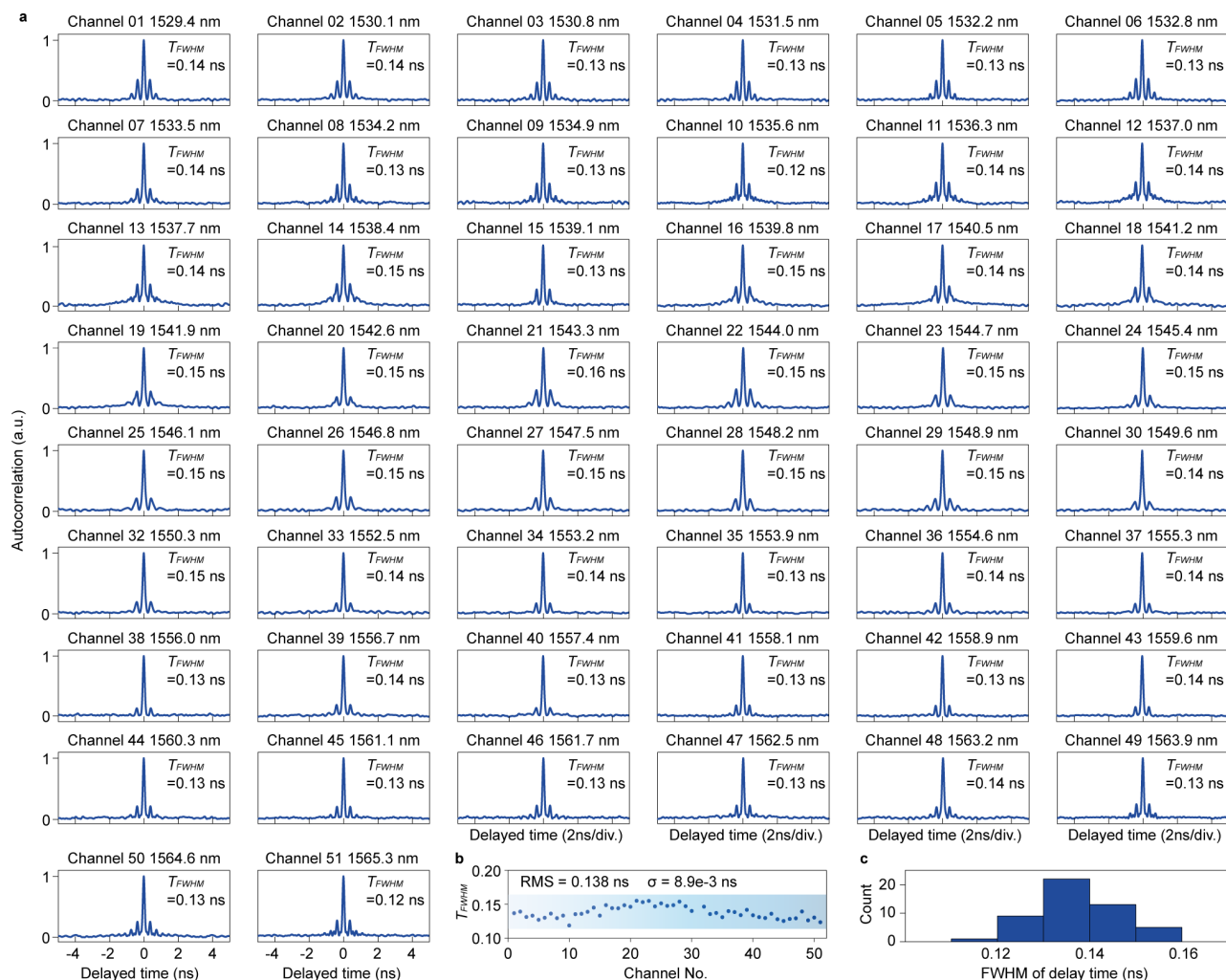
Supplementary Fig. 3: 50-channel auto-correlation analysis. a, Measured auto-correlation results of the chaotic microcomb source within the range from 1529.4 nm to 1565.3 nm. **b**, FWHM distribution and **c**, statistical analysis of the 50-channel auto-correlation traces.

Channel-by-channel characterizations are performed for the 90 GHz chaotic microcomb used for 3D imaging under the same pump detuning around 1551.7 nm, as shown in Supplementary Fig. 3a. A programmable optical spectral shaper is used for each single channel selection. The auto-correlation of the selected channel is then calculated via its time domain waveform (totally 12.5 μs) recorded by a real-time oscilloscope under the sample rate of 80

7

GSa/s. The results show great inter-channel consistency of all 51 comb lines. Supplementary Fig. 3b and c shows the FWHM distribution and statistical analysis of the measured auto-correlation results, respectively. All the auto-correlation FWHM lie within 0.12 ns to 0.15 ns, which correspond to the theoretical range resolution of 1.8 cm to 2.25 cm. The root mean square for the auto-correlation FWHM is around 0.139 ns, with a standard deviation of 8.9 ps.

# IV. SUPPLEMENTARY NOTE IV: PARALLEL 3D IMAGING FOR CHARACTERISTIC OF RANGE RESOLUTION
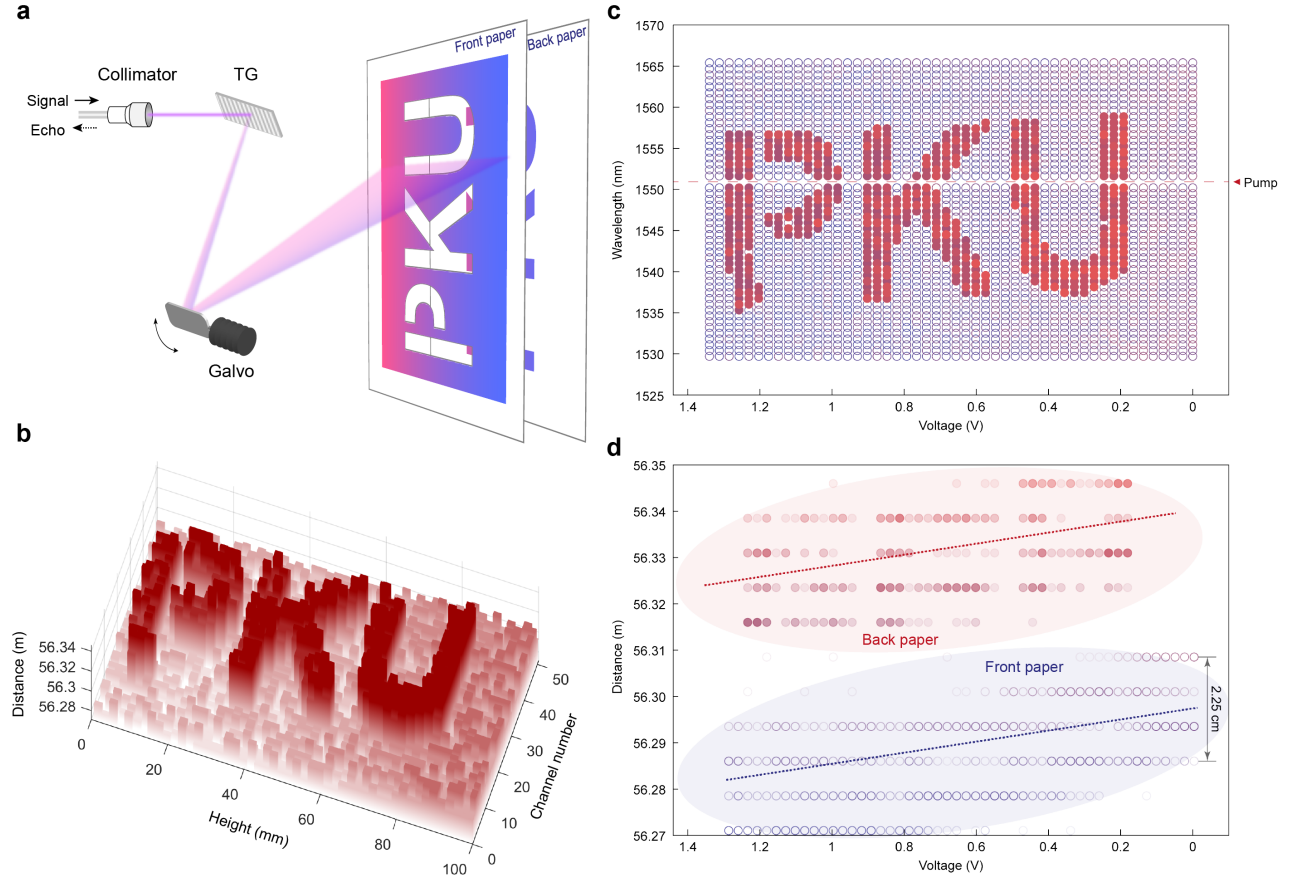
Supplementary Fig. 4: Parallel 3D imaging of 50 channels of the chaotic comb for the characteristic of range resolution. a, a brief illustration of the experiment setup without showing the chaotic comb generator, reference end and receiving end. **b**, The rebuilt point cloud of the Peking university logo by vertical scanning. The spacing between the two sheets of paper is about 2 cm. **c**, Top-view and **d**, Side-view of the point cloud. The two sheets of paper are placed at a slight angle, which is illustrated by two dashed lines. The purple dashed denotes the front paper, and the red dashed line denotes the back paper. The horizontal axis in **c** and **d** is the static tuning voltage of the galvo mirror, which can be converted to the height axis in **b**. Note that the round trip distance is recorded in **b** and **d**, which is twice the actual distance.

Based on the consistent range resolution of the chaotic comb lines (see in supplementary note

III), we also perform a parallel 3D imaging experiment. As shown in Supplementary Fig. 4a, the target is consist of two sheets of white papers with a spacing of 2 cm, which is within the range of the theoretical range resolution. The front paper is hollowed out by a vertically aligned Peking University logo, while the back paper serves as the background. Thus, the detection points located on the back paper can represent the logo. The experiment is set up as in the main text, that 50 carriers of the chaotic comb are radiated to measure the target at a distance of approximately 1.6 m from the collimator. Supplementary Fig. 4b illustrates the reconstructed point cloud with a image resolution of 50×50 pixels. From the sideview of the parallel imaging results (see in Supplementary Fig. 4d), it can be observed that the detection points representing the PKU logo can be well distinguished even when the two sheets of paper are set at a slight angle, and there is a clear boundary among the detection points on the front paper (red solid circles) and those on the back paper (purple hollow circles). The deviation of the detection points on the same paper is in good agreement with the the theoretical range resolution. A sampling rate up to 80 GSa/s is employed here and in the main text, to ensure the ranging accuracy.

V. SUPPLEMENTARY NOTE V: REFLECTION INDEX DETECTION
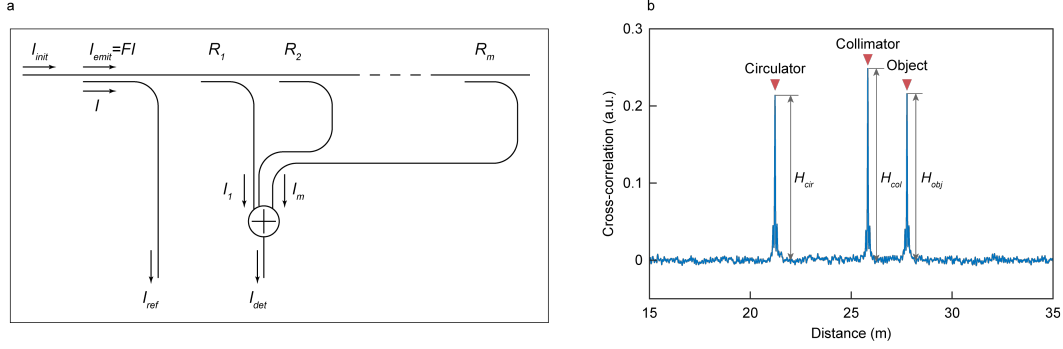
Supplementary Fig. 5: Principle of the reflection detection. a, the schematic diagram of the Lidar system. **b**, the cross-correlation between the reference signal and detected signal obtained in experiment. The peaks resulting from the circulator, collimator and the object are marked with text.

The detection principle is given in Supplementary Fig. 5a. The initial chaotic source is divided into two arms, one for reference and the other for reflection detection. The signal I_{emit} for detecting is F times larger than that for referring. As I_{emit} propagating in a space, partial signal will be reflected due to some scatterers and reflectors with the reflection index of R_m. All reflected signal I_m will be collected at the receiver port as I_{det}, expressed as

$$I_{\text{det}}(t) = \sum_m I_m(t) \tag{3}$$

$I_m(t)$ is equal to $R_m F I(t - \tau_m)$, where τ_m is the delay time between the emitted signal I_{emit} and the received signal I_m. Summarily, the reference signal can be expressed as $I_{ref}(t) = I(t - \tau_{ref})$, where τ_{ref} is the delay time between I_{ref} and I.

Supposing the I_{init} as an ideal chaotic signal whose ACF is a dirac function, the distance and reflection index can be extracted, employing the cross-correlation between the reference signal I_{ref} and the detected signal I_{det}:

$$
\begin{aligned}
R_{ref,det}(\tau) &= \langle I_{ref}(t + \tau) I_{det}(t) \rangle_t \\
&= F \sum_m R_m \langle I(t + \tau - \tau_{ref}) \cdot I(t - \tau_m) \rangle_t \\
&= F \sum_m R_m \delta(\tau - \Delta \tau_m)
\end{aligned}
\tag{4}
$$

11

The relatively delay time $\Delta\tau_m = \tau_{ref} - \tau_m$ have a linear relationship with the space distance, used to range, as illustrated in the main text. If several echo signals existed and detected, which is the circumstance of our detection, the relative reflection index can be extracted by comparing the heights of correlation peaks of different objects. Supplementary Fig. 5b shows the cross-correlation function calculated based on our experiment data. Three peaks can be detected, resulting from the reflection of fiber circulator before the collimator, the collimator and the object to detect. The reflection indexes of circulator and collimator can be regarded as known parameters. Fig. 4e gives the ratio of H_{obj} to H_{col}, where H_{obj} and H_{col} are the heights of correlation peaks resulting from the detected object and the collimator. Such internal reflection in a signal channel mainly comes from the monostatic detection setup where the probing signal and the backscattered light share the same collimator. It can be reduced by more deliciated engineering efforts, for example, by using two collimators to separate the optical path of the probing signal and the backscattered light, so that the reflection from the transmitting collimator can be eliminated and the circulator can also be removed.

## VI. SUPPLEMENTARY NOTE VI: THE RANGE RESOLUTION OF THE CHAOTIC COMB
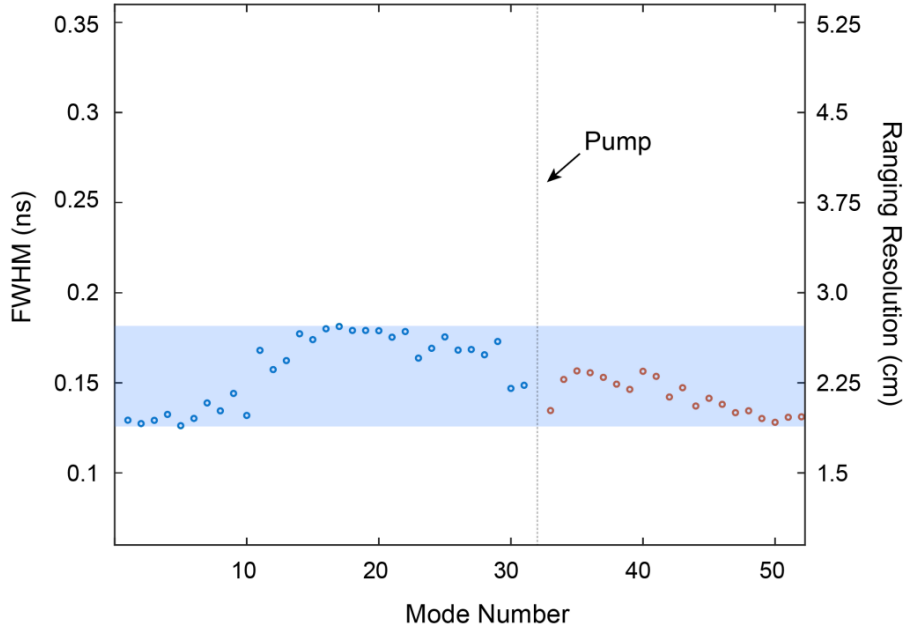
Supplementary Fig. 6: Relationship between FWHM of the ACF for each comb line (except the pump, the grey dashed line) when the detuning between pump laser and cavity resonance is 40 GHz. The blue hollow circles indicate the comb lines at the left of the pump, while the red hollow circles indicate those at the right of the pump.

We use the average range resolutions of all selective comb lines to express the range resolution of the whole system. Since the principle of the chaotic ranging is realized by correlating the probing signal reflected or back scattered from the target with a delayed reference, the bandwidth of the optical chaos will directly determine the range resolution. According to the Wiener-Khinchin theorem, the Fourier transform of the auto-correlation function (ACF) is the power spectrum density, thus wider chaotic bandwidth means better range resolution. We use the FWHM of the autocorrelation results of each comb line to quantitatively express the range resolution. In Fig.2g of the main text, we have experimentally shown the FWHM of the ACF for each comb line, which reflects the bandwidth of the comb lines. The plot below (the blue region in Supplementary Fig. 6) shows the experimental FWHM of the ACF for all 51 selective comb lines and the corresponding range resolution is $2.3 \pm 0.4 cm$.

The small deviation indicates that all probe channels share almost the same range resolution when the detuning between pump laser and cavity resonance is properly set. This feature has important practical significance that the non-degradation of the ranging performance for parallel LiDAR can ensure high confidence detection of spatial points in all directions.

# VII. SUPPLEMENTARY NOTE VII: CHAOTIC COMB DRIVEN BY A DFB LASER
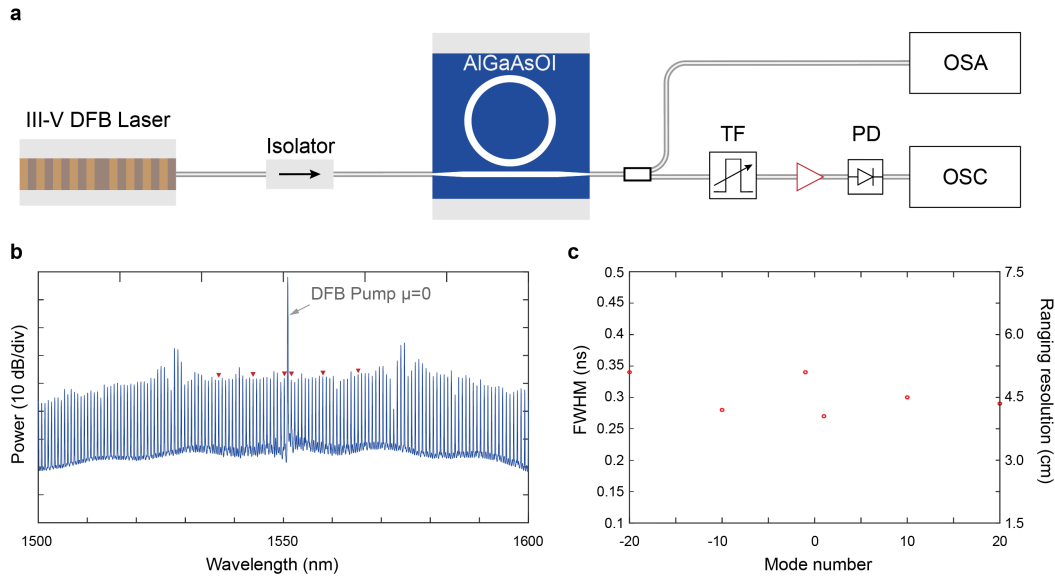
Supplementary Fig. 7: Generation of the chaotic comb driven by a DFB laser. **a**, Experimental setup of the chaotic comb generator under the condition of a DFB pump. The output power of the DFB laser is 18.7 dBm. TF: Tunable bandpass filter; OSA: Optical spectrum analyzer; OSC: Optical sampling oscilloscope. **b**, The optical spectrum of the generated chaotic comb with the on-chip pump power of about 20 mW. **c**, The autocorrelation function of the six selective channels with mode numbers of $\pm 1, \pm 10, \pm 20$, which are illustrated by red arrows in **b**.

In this section, we demonstrate the generation of the chaotic comb driven by a III-V DFB laser. Although the on-chip pump power is about 20 mW, a broadband chaotic comb with flat-top spectrum in the central part can still be generated by manually tuning the frequency of a DFB laser. In order to reflect the range resolution of the comb, we randomly select six comb channels (mode number $\mu = \pm 1, \pm 10, \pm 20$) and characterize their range resolutions. Supplementary Fig. 7c shows that there is a fluctuation in the range resolution (3.6-5.1 cm) of the comb channels, which results from the relatively low pump power. By increasing the laser-to-chip coupling efficiency, this fluctuation can be much suppressed and the average range resolution will also be improved.

# VIII.   SUPPLEMENTARY NOTE VIII: DISCUSSION ON RANGING PRECISION
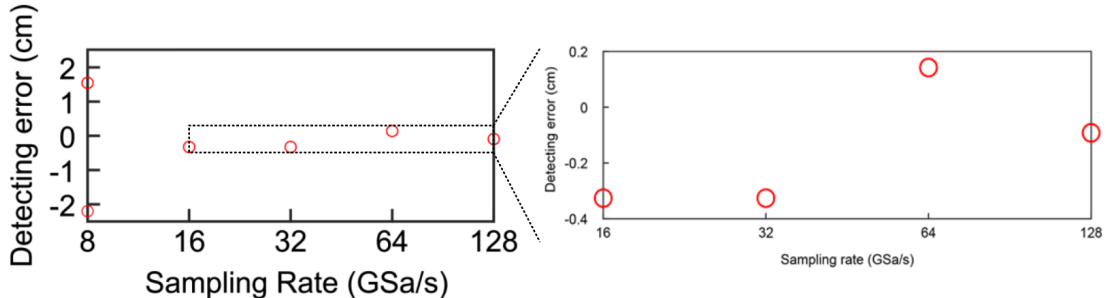
Supplementary Fig. 8: Relationship between ranging precision and sampling rate of the digital oscilloscope. For each selection of the sampling rate, the round-trip length between the collimator and target board is recorded and the ranging test is performed 50 times. The zoom-in of detection error variation is shown on the right panel.

The ranging precision in our parallel chaotic LiDAR is estimated as follows:

$$\Delta R = \frac{1}{2}c\tau_{sampling} \tag{5}$$

Where c is the optical velocity, and $\tau_{sampling}$ represents the sampling rate of the digital oscilloscope. In the ranging demo, we amplify the echo signal at the receiving end and use a detector with a broadband response larger than the chaotic spectrum, so the influence from the amplifier and photodetector can be ignored. The time delay between the reference and target signals is calculated by determining the peak of waveform cross-correlation, which will be directly restricted by the sampling time. Since the sampling rate up to 80 GSa/s is employed in the main text, the calculated ranging precision is about 2 mm. Besides, we also perform the ranging test of the same target and obtain the distance using different sampling time. As shown in Supplementary Fig. 8, in the absence of interpolation, the ranging precision will be degraded as the sampling rate decreases, and a ranging precision of less than 2 cm can be realized when the sampling rate is above 8 GSa/s. By introducing interpolation, this accuracy can also be ensured with a lower sampling rate even down to 1.25 GSa/s [9, 10].

IX. SUPPLEMENTARY NOTE IX: RANGE ACCURACY UNDER DIFFERENT COMB STATES
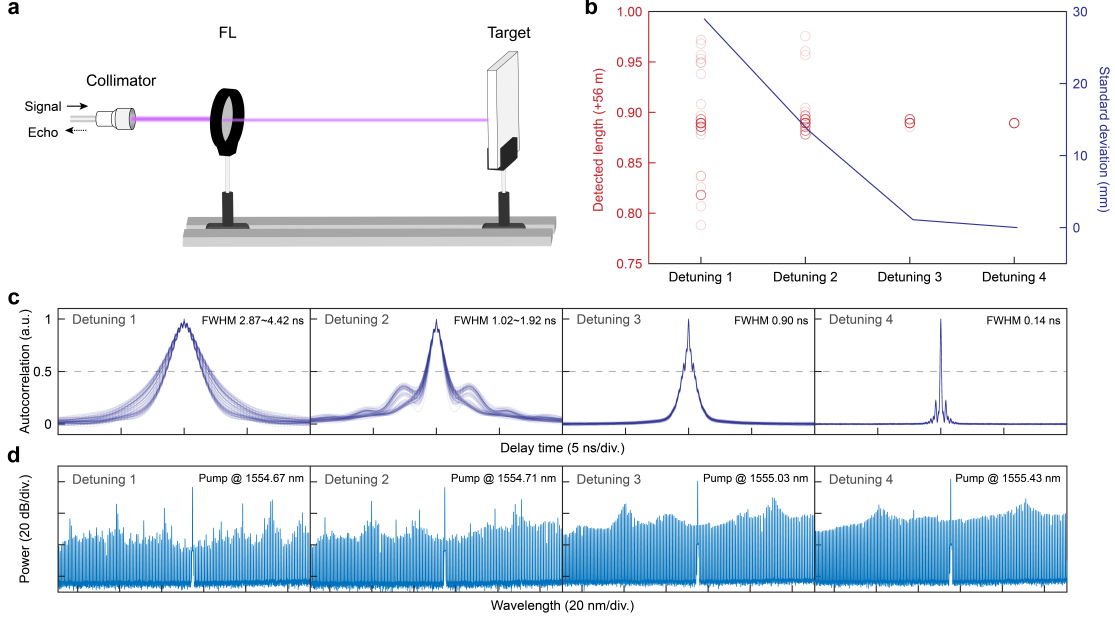
Supplementary Fig. 9: Variation of range accuracy throughout the evolution of pumping laser sweeping into the resonance. a, Illustration of the ranging measurement. Labels: FL, focusing lens; **b**, variation of detected length and the standard deviation of the distance error as the pump detuning increases; **c**, the auto-correlation function (ACF) of the probe channel under different comb states; **d**, spectrum distribution of four different comb states.

In [10], the random-modulation continuous-wave lidar is analyzed and a distance standard deviation approximation is given as

$$\sigma_D \approx \frac{cT_c}{2SNR} \tag{6}$$

Where T_c is related to the width of correlation peaks and SNR is signal-noise-ratio. Thus, the accuracy is proportional to $FWHM/SNR$, similarly to that of FMCW Lidar estimated in [11]. In order to demonstrate the variation of range accuracy throughout the evolution of pumping laser sweeping into the resonance, four chaotic comb states are recorded during the increase of the pump detuning. For each comb state, we use the optical bandpass filter

to extract one comb line as the probe channel to detect the distance to the whiteboard, as shown in Supplementary Fig. 9a. As the pumping laser is swept into the resonance (shown in Supplementary Fig. 9c), more power is injected into the microresonator, which leads to higher power density in the cavity. The undulating spectrum becomes gradually flattened and the corresponding ACF FWHMs become narrower, which helps suppress the distance standard deviation and improve the range accuracy. 100 times measurements are performed under each pump detuning (Detuning 1-4) and the standard deviation of the distance error is calculated by using the measured distance at detuning 4 as the reference since we have demonstrated in Supplementary note XII that our comb-based LiDAR system working at a large detuning has been characterized to have extremely good accuracy. As shown in Supplementary Fig. 9b, a dramatic improvement in range accuracy with the detuning can be observed when the pump detuning increases, which results in an order of magnitude decrease in the standard deviation of the distance error.

X.   SUPPLEMENTARY NOTE X: RELATIONSHIP BETWEEN SNR AND MEA-SUREMENT ERROR WITH DETECTION DISTANCE
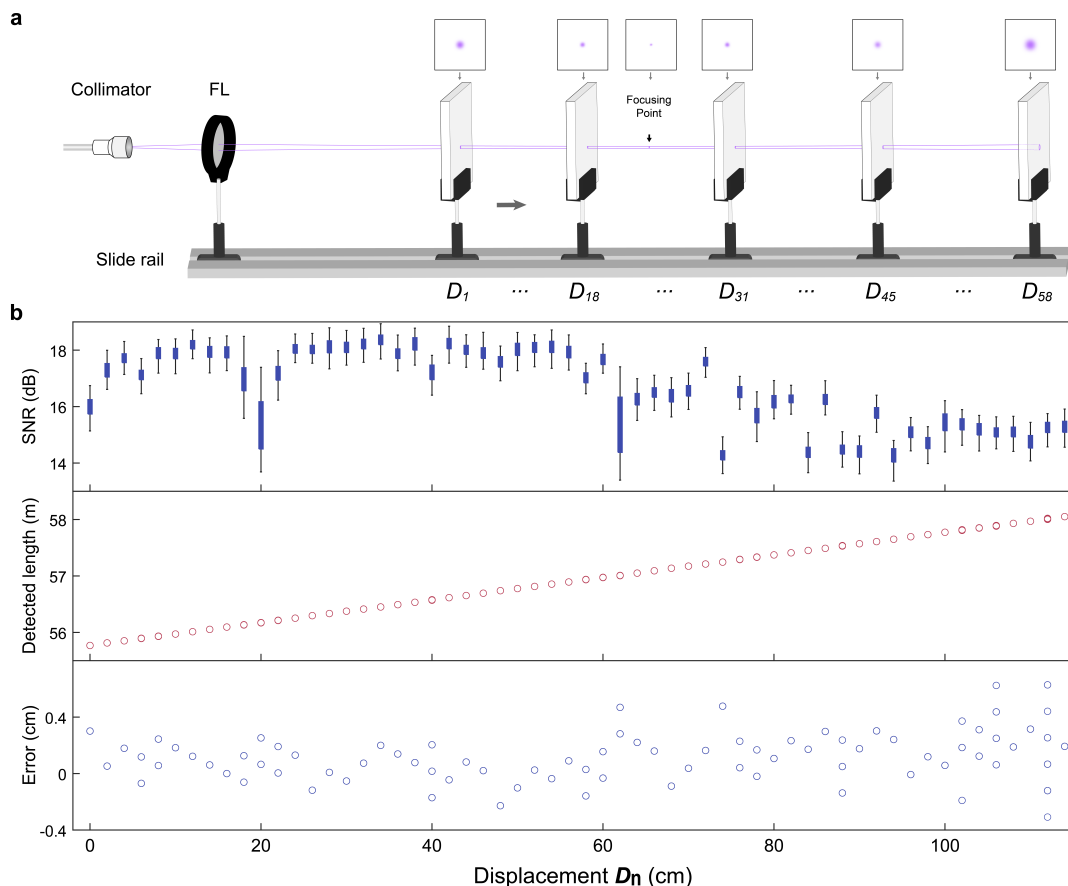
Supplementary Fig. 10: Relationship between range accuracy and relative displacement. a, Illustration of the ranging measurement. The size variation of the light spot along the displacement is shown in the top panel, which demonstrates the variation of the beam divergence. Labels: FL, focusing lens; **b**, the variation of cross-correlation SNR, round-trip length, and round-trip range error with respective detected positions (58 measuring points in total, D_{1-58}).

One channel of the chaotic comb was filtered out as the transmit signal, and the measured target was placed on a sliding rail with a scale. We change the target distance in 2 cm steps each time and test the distance of each position 90 times. In Supplementary Fig. 10a, since the starting position of the measured distance is set before the focal point of the focusing lens in our experiment, the measured target gradually approaches the focal point and then

19

moves away from it as the detection distance increases. As shown in Supplementary Fig. 10b, because the spot at the focal point is the smallest, the SNR and range accuracy of the received signal measured at this position are the best. However, at the position far from the focal point, the beam divergence makes the spot larger, and the signal power received by the system receiver is degraded, resulting in a decrease in cross-correlation SNR and detection accuracy. Moreover, the area of 2 mm range accuracy lies roughly in the interval of 40 cm-60 cm displacement, where the degradation in SNR and measurement error at some test points results from the slight inclination of the target surface affecting the receiving power.

XI. SUPPLEMENTARY NOTE XI: DISCUSSION ON THE EFFECTIVE RANGE AND QUALITY DEGRADATION OF 3D IMAGING

A general standard of the LiDAR effective range analysis can be processed by recording the distance until the signals at the detection threshold will be detected with 50 % probability [12]. The receiving power of the LiDAR system P_{RX} for an underfilled target (In which case all of the energy in the laser pulse is scattered by the target) can be expressed by

$$P_{RX} = P_{TX}\eta_{TX}\frac{\rho A_{RX}}{4\pi D^2}\eta_{RX} \tag{7}$$

Where P_{TX} is the output power of the transmitter; η_{TX}/η_{RX} represents the emission and receiving efficiency, respectively; A_{RX} is the area of the receiving aperture; ρ is the reflectance of the measured target; D is the depth of the target. Here, we evaluate the effective range and quality variation of 3D imaging at different distances by attenuating the power of the emitted light. In the experiments, we attenuate the emitted light power by 2 dB at a time and subsequently perform a 3D imaging of a whiteboard with a pixel value of 10 × 10. As shown in Supplementary Fig. 11a, the signal-to-noise ratio (SNR) of each pixel has a relatively stable distribution above 10 dBm, but when the power continues to decay, it can be observed that the SNR starts to degrade obviously as the power decreases. The probability of detection (similar to the detection reliability), which can be approximately obtained by the ratio between the number of the successfully detected points and the total number of the testing points, starts to fall off as the attenuation is larger than 10 dB and drops to only 50 % when the attenuation is 20 dB, which is equivalent to increasing the ranging distance to 10 m. If we neglect the loss of receiving efficiency, the effective range for our LiDAR system prototype can approximately achieve 10 m, where the average signal levels are equal to the detection threshold. Supplementary Fig. 11b indicates that the 3D mapping consistency deteriorates as the power attenuation increases and the standard deviation of the 3D imaging results from below 1 mm rises to 2.7 mm at an equivalent detection length of 10 m.

Despite the above performance decay, the increase in the integration time of the photodetector can help further improve the cross-correlation SNR and probability of detection. Comparing the experimental results shown in Supplementary Fig. 12 with those in Supplementary Fig. 11a, the SNR and detection reliability under 20 dB can be greatly improved by increasing the integration time from 12.5 μs to 125 μs.
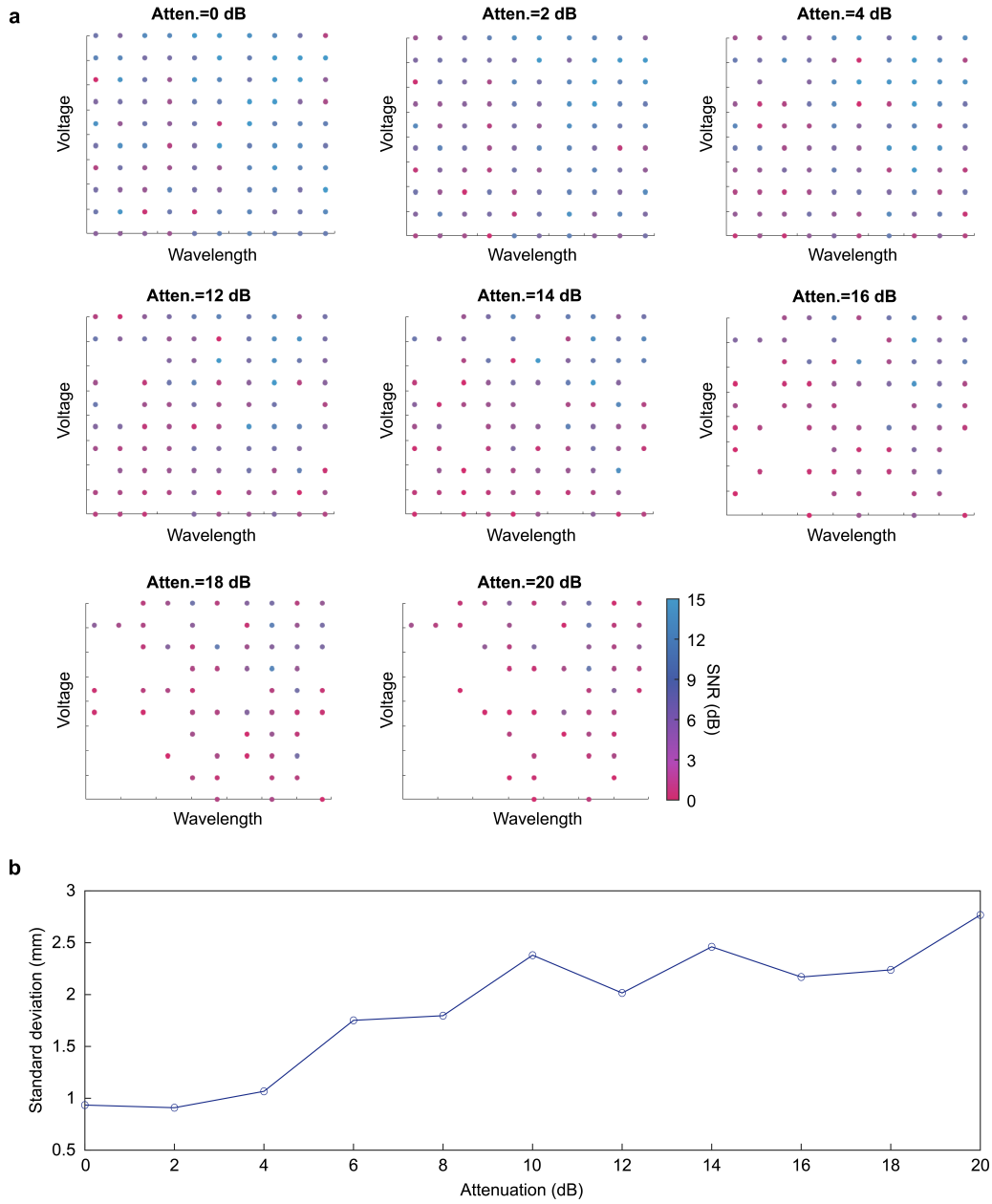
Supplementary Fig. 11: Quality variation of 3D imaging under different power degradation. a, the variation of SNR and detection reliability with the power attenuation. The horizontal axis represents the channel wavelength. The vertical axis represents the control voltage added to the galvo mirror; **b**, the relationship between the standard deviation of the 3D imaging spots and the power attenuation.
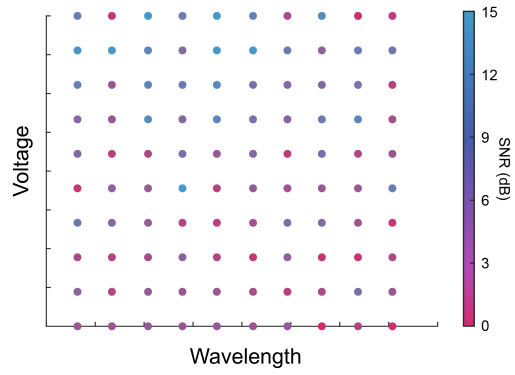
Supplementary Fig. 12: SNR and detection reliability under 20 dB attenuation using the integration time of 125 μs.

XII. SUPPLEMENTARY NOTE XII: CHARACTERISTIC OF THE RANGE ACCURACY OF CHAOTIC LIDAR SYSTEM
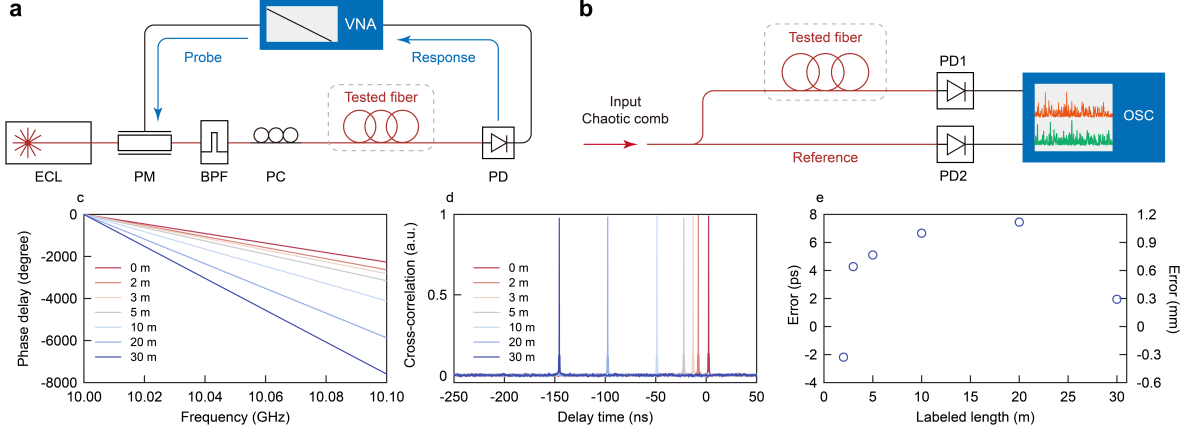
Supplementary Fig. 13: Measurement of time delay in fibers. a, Test link based on optical vector analysis (OVA). **b**, test link based on chaotic ranging employing one chaotic comb line. **c**, measured phase delay by OVA. **d**, calculated cross-correlation functions for different lengths of fibers. **e**, ranging error based on chaotic combs compared with OVA. Labels: ECL, external cavity laser; PM, phase modulator; BPF, bandpass filter; PC, polarization controller; PD, photodetector; VNA, vector network analyzer; OSC, oscilloscope.

In Fig. 3c, the ranging accuracy is verified by continuously detecting the displacement of a white sheet moving 1 cm each time. In this part, the ranging accuracy is also verified by comparing with an optical vector analysis (OVA) [13, 14] method to measure the time delay in fibers with different lengths. Supplementary Fig. 13a shows the test link based on OVA. The time delay is extracted by testing the phase response of the microwave signal loaded on the carrier laser by a phase modulator. Considering a phase response $\phi(\omega)$ of the link to be tested, the delay time τ in the link can be calculated by

$$\tau = d\phi(\omega)/d\omega \tag{8}$$

where ω is the modulation frequency loaded on the phase modulator. To ensure the effective detection of the microwave signal, a bandpass filter is arranged after the phase modulator, to suppress the lower sideband. In the experiment, one fiber labeled with a length of 0.5

m is always arranged between the polarization controller and the photodetector, and fibers labeled with different lengths (2 m, 3 m, 5 m, 10 m, 20 m, and 30 m) are connected with the 0.5 m fiber and the photodetector. Supplementary Fig. 13c shows the measured phase delay and the time delay is obtained by linear fitting the measured phase delay to estimate the slope. Supplementary Fig. 13b shows the test link based on OVA. One comb line is selected and injected into the test link. The input signal is separated into two arms where one is connected with fibers to be tested and the other is used for reference. The arrangement of the tested fiber is the same as that in the test link based on OVA, where fibers labeled with different lengths are linked with the 0.5 m fiber and a photodetector. Calculating the cross-correlation between the recorded signal by the oscilloscope, we can obtain the time delay. Supplementary Fig. 13d shows the calculated cross-correlation functions for fibers with different lengths. Subtracting the time delay with 0.5 m fiber, we can get the time delay in tested fibers. Supplementary Fig. 13e shows the difference between the two methods. Agreeing with the result in Fig. 3, the ranging accuracy employing chaotic combs is better than 2 mm, indicating a high performance.

XIII. SUPPLEMENTARY NOTE XIII: HIGH INTERFERENCE-TOLERANT WITH THE ASE JAMMING SIGNAL
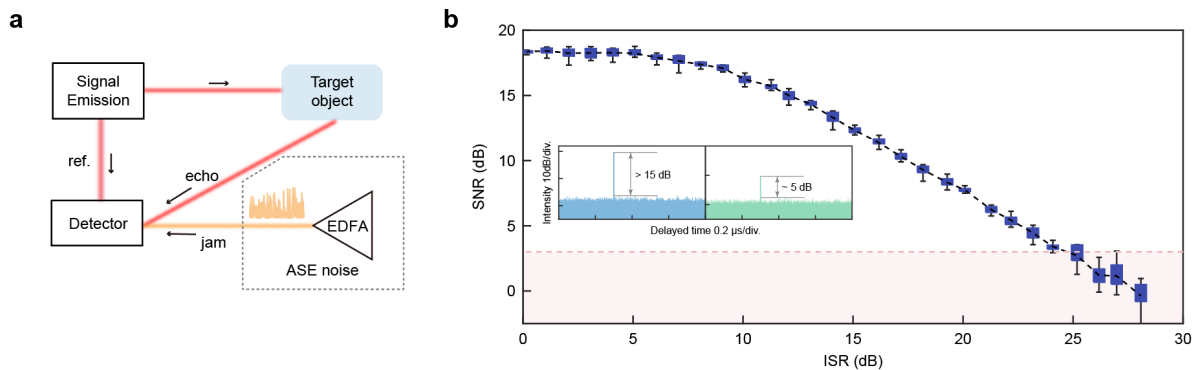
Supplementary Fig. 14: Ranging under the ASE jamming signal. a, The experimental setup for anti-jamming characterization of the ASE noise. **b**, the calculated cross-correlation peak SNR with the variations of Interference-Signal ratio (ISR). The boxplots are derived from the number of tests N=10, respectively. The horizontal line indicates the median, the box spans 0.25 to 0.75 quartile, and the whisker length corresponds to 1.5 times the interquartile range. Inset: correlation results when interference signal intensity is 10 times and 100 times higher than the target echo, respectively.

As shown in Supplementary Fig.   14a, we perform an experiment to verify the high interference-tolerant capability of our chaotic comb with the ASE noise, where the ASE jamming signal is generated by an EDFA and mixed with the chaotic echo signal ahead of the receiver. To avoid saturating the receiving photodetector, we attenuate the power of the echo signal component for the variation of ISR. From the cross-correlation results depicted in Supplementary Fig. 14b, the SNR is flat and saturated when the ISR is below 5 dB and then decreases linearly as the interference power increase. A correlation-peak-detectable ISR of 25 dB can be obtained when the SNR is beyond the 3 dB threshold, which shows that our chaotic LiDAR system can resist the ASE interference even when the jamming power is 200 times higher than that of the echo signal.

[1] Herr, T. *et al.* Temporal solitons in optical microresonators. *Nature Photonics* **8**, 145–152 (2014).

[2] Herr, T. *et al.* Universal formation dynamics and noise of kerr-frequency combs in microresonators. *Nature Photonics* **6**, 480–487 (2012).

[3] Carmon, T., Yang, L. & Vahala, K. J. Dynamical thermal behavior and thermal self-stability of microcavities. *Optics Express* **12**, 4742–4750 (2004).

[4] Li, Q. *et al.* Stably accessing octave-spanning microresonator frequency combs in the soliton regime. *Optica* **4**, 193–203 (2017).

[5] Guidry, M. A., Lukin, D. M., Yang, K. Y., Trivedi, R. & Vučković, J. Quantum optics of soliton microcombs. *Nature Photonics* **16**, 52–58 (2022).

[6] Zheng, Y. *et al.* Integrated gallium nitride nonlinear photonics. *Laser & Photonics Reviews* **16**, 2100071 (2022).

[7] Liu, X. *et al.* Aluminum nitride nanophotonics for beyond-octave soliton microcomb generation and self-referencing. *Nature Communications* **12**, 1–7 (2021).

[8] Liu, J. *et al.* High-yield, wafer-scale fabrication of ultralow-loss, dispersion-engineered silicon nitride photonic circuits. *Nature Communications* **12**, 1–9 (2021).

[9] Cheng, C.-H. *et al.* 3d pulsed chaos lidar system. *Opt. Express* **26**, 12230–12241 (2018).

[10] Ai, X., Nock, R., Rarity, J. G. & Dahnoun, N. High-resolution random-modulation cw lidar. *Applied optics* **50**, 4478–4488 (2011).

[11] Baumann, E. *et al.* Speckle phase noise in coherent laser ranging: fundamental precision limitations. *Optics letters* **39**, 4776–4779 (2014).

[12] Lidar effective range. Https://www.allegromicro.com/en/insights-and-innovations/technical-documents/p0177-lidar-effective-range.

[13] Zhu, C. *et al.* Silicon integrated microwave photonic beamformer. *Optica* **7**, 1162–1170 (2020).

[14] Qing, T., Li, S., Tang, Z., Gao, B. & Pan, S. Optical vector analysis with attometer resolution, 90-db dynamic range and thz bandwidth. *Nature communications* **10**, 1–9 (2019).